

## **Microtubule Structure at 8 Å Resolution**

**Huilin Li, David J. DeRosier<sup>1</sup>, William V. Nicholson,  
Eva Nogales<sup>2</sup>, and Kenneth H. Downing\***

**Life Sciences Division  
Lawrence Berkeley National Laboratory  
Berkeley, California 94720**

<sup>1</sup> Department of Biology and The Rosenstiel Basic Medical Sciences Research Center, Brandeis University, Waltham, Massachusetts 02454

<sup>2</sup> Howard Hughes Medical Institute, Department of Molecular and Cell Biology, University of California, Berkeley, California 94720

Correspondence should be addressed to KHD:

Donner Laboratory, Lawrence Berkeley National Laboratory, Berkeley, California 94720

tel: 510-486-5941

fax: 510-486-6488

e-mail: [kdowning@lbl.gov](mailto:kdowning@lbl.gov)

## Summary

We have obtained a 3-D reconstruction of intact microtubules, using cryo-electron microscopy and image processing, at a resolution of about 8 Å, sufficient to resolve much of the secondary structure. Rather than use helical image processing methods, we have treated the microtubule images as strings of single particles. Since the structures of the alpha and beta monomers are so similar at this resolution, we can ignore the difference between them. The resulting map is thus an average of the alpha and beta tubulin structures. The level of detail in the map allows docking of the tubulin crystal structure with very strong constraints, providing several important insights not previously available through docking tubulin into lower resolution maps. This work provides an improved picture of the interactions between adjacent protofilaments that are responsible for microtubule stability and also suggests that some structural features are different in microtubules from those in the zinc sheets in which the tubulin structure was determined. The N-terminal loop is a major partner in forming the inter-protofilament interface with the M-loop. The small H6 domain is less involved in inter-protofilament contacts than in the crystals, and may be flexible enough to allow regulatory ligands such as Taxol to diffuse through the microtubule wall and bind to the inside surface. A cluster of residues that differ among beta tubulin isotypes is located at the site of major inter-protofilament interactions, which may relate to differences in dynamic properties and drug sensitivities observed for the different isotypes.

## Introduction

Microtubules play fundamental roles throughout the life of eukaryotic cells. These roles often depend on the dynamic instability of microtubules and its regulation by cellular factors. The dynamic behavior of microtubules has been the subject of great interest for several decades, but only recently has the structure of tubulin allowed us to begin to understand the molecular basis of the dynamics. In order to advance our knowledge of the regulation of the microtubule cytoskeleton, it is essential that we develop a better understanding of the interactions among the tubulin subunits within a microtubule. The structure of the intact microtubule which we report on here reveals new inter-protein interactions and conformational features associated with the formation of microtubules.

The structural unit of a microtubule is the  $\alpha$ - $\beta$  tubulin heterodimer. The structure of the dimer was determined by electron crystallography using crystalline sheets of tubulin that form in the presence of zinc ions<sup>1</sup>. Alpha and beta tubulins share about 40% sequence homology, and as expected, their structures are very similar. Indeed, at a resolution around 6 Å, the structures appear essentially indistinguishable<sup>2</sup>, although at higher resolution differences in side chains and some differences in secondary structure are identified.

Dimers connect head-to tail to form protofilaments (pf), and protofilaments assemble side by side to form the microtubule. Both *in vivo* and under most conditions *in vitro*, most microtubules have 13 protofilaments, although this number can vary from 9 to 16<sup>3</sup>. The protofilaments in most microtubules follow a helical path around the microtubule axis with a long pitch, often called the superhelix, but in microtubules with 13 protofilaments they are parallel to the microtubule axis with no helical twist. This special feature is fully exploited in our microtubule image processing procedure. The monomers follow a shallow, left-handed helix. In most microtubule types, including those with 13 protofilaments, this helix rises by three monomers in one turn around the axis, producing what is termed a 3-start helix. Since the rise corresponds to one and a half dimers, there is a seam running along the length of the microtubule where different types of monomers become neighbors. Thus 13-pf microtubules are

not strictly helical in the sense of all heterodimers being related by the helical symmetry. In fact, only a few of the naturally occurring microtubule types, such as 12-pf, 2-start; 15- and 16-pf, 4-start types, have such symmetry and are amenable to helical image processing. If the differences between alpha and beta are ignored, though, all microtubules can be considered true helices. The 13-pf microtubules, though, are degenerate helices, as their protofilaments run parallel to the axis. The Fourier transform of a helix consists of a set of layer lines, each populated with a set of Bessel functions that derive from the helix structure. In conventional helical image processing, values for the Bessel functions are determined from Fourier transforms of images and are used to compute the helix structure. In the case of 13-pf microtubules, however, layer lines contain overlapping Bessel functions of different order, which adds a degree of complication in analyzing images using helical methods.

While there have been a number of notable successes in reconstructing microtubules and motor-decorated microtubules by helical methods<sup>4-8</sup>, the resolution has generally been limited to 15 – 20 Å. Back projection methods have also been used in motor-decorated microtubule reconstructions, taking advantage of the helical nature of the microtubule to obtain a 3-D representation from a single image<sup>9,10</sup>. While this approach has even allowed identification of the seam in some of the non-helical microtubule types, it has not yet yielded higher resolution than the helical methods.

Structural information about the lateral contacts between protofilaments is of special importance in understanding the dynamics and regulation of microtubule assembly and disassembly. In particular, disassembly of the microtubule is generally understood to result from a weakening of the lateral interactions, and we would like to understand in detail both the nature of these interactions and their possible transitions. The atomic structure of tubulin, which was determined from two-dimensional crystals of protofilaments, did not provide information about the lateral interactions between protofilaments in microtubules. In the crystals, the protofilaments are antiparallel whereas in microtubules they are parallel. While the longitudinal, intra-protofilament interactions in the two structures are assumed to be the same, the lateral interactions between the protofilaments must be completely different. In addition, there may also be conformational differences in tubulin between the two polymers. We obtained a first

model of the microtubule by docking the atomic structure for the protofilament into a microtubule reconstruction that had a nominal resolution of about 20 Å<sup>11</sup>. The fit of the model within the molecular envelope was very good, giving information about the relative orientations and interactions between adjacent dimers. More recently, reconstructions at higher resolution<sup>8,12</sup> allowed some refinement of the docking. However, none of these reached the sub-10 Å resolution necessary to identify elements of secondary structure and thereby to characterize conformational differences between the zinc-sheet and microtubule protofilaments.

Advances in the methodology of single particle reconstructions have made it feasible to consider this approach to obtaining resolution better than 10 Å with microtubules, treating each image as a string of single particles. This approach allows one to take account of distortions within a single microtubule that limit resolution with helical processing. Using a combination of single particle and crystallographic methods, we have obtained a microtubule reconstruction at 8 Å resolution. Most of the alpha helices in the dimer structure can be identified in this map, providing a very strong constraint in placement of the atomic structure. This docking gives an improved picture of the inter-protofilament interactions and suggests some conformational differences in tubulin between microtubules and Zn-sheets.

## Results

### *Microtubule images and CTF determination*

The selection of microtubules with a defined number of protofilaments from high-contrast images, such as negatively stained or highly defocused cryo-images, is fairly straightforward. The superposition of protofilaments on the top and bottom of a microtubule produces a distinctive Moiré pattern in the projection image that can be used to determine the type of most microtubules<sup>3</sup>. However the contrast in our low-defocus images recorded at 400 kV (Fig. 1) is too low to allow visual identification of the microtubule type, so selection was based on optical Fourier transforms. Generally, selection was based on the strength and completeness of the second layer line. In the best images, the optical diffraction extended to the

fourth layer line at 10 Å. In principle, the lack of layer line splitting in the off-meridional part of the Fourier transform, corresponding to the Moiré pattern in the image, should be sufficient to identify the 13-protofilament microtubules. However, there was not always sufficient signal-to-noise to eliminate non-13-protofilament microtubules, and there were occasional transitions in the number of protofilaments along a single microtubule as well as other defects<sup>13</sup>. Thus a second selection was performed on the microtubules after digitization. Images were compressed by a factor of four along the axis and filtered to enhance the visibility of the protofilaments in order to judge by eye whether they contained 13 protofilaments along the entire length.

Correction for the contrast transfer function (CTF) was done before image alignment. The power spectra for all of the segments along a single microtubule were summed, and the defocus for each micrograph was determined from a plot of the radial average of the sum of power spectra. To enhance the clarity of the Thon rings, the power spectra were band-pass filtered, resulting in a smoother rotational average that could be fit with an error in the defocus of less than 500 Å. This provides an accurate determination of the CTF out to about 7 Å.

*Rotational alignment, magnification scaling and segment averaging in the generation of a 10 Å map*

Even in the best images the microtubules undergo a significant in-plane curvature that must be corrected before combining segments. In most helical image processing, this is done by fitting a curve along the center of the object, and then straightening the image by interpolation based on a spline fit to the curve<sup>14</sup>. Our approach was to rotationally align each short segment individually. We found that the orientation could be efficiently determined using a Radon transform of the power spectrum of the segment. Radon transforms have been applied for the alignment of single particles in previous electron microscopy work<sup>15,16</sup>. For a 2-D image, the discrete Radon transform often called a sinogram, is a series of projections along different angles. With a helical specimen, projection of the Fourier transform along the direction of the layer lines produces a set of distinct peaks that are identified with a high signal-to-noise ratio.

Figure 2 illustrates the alignment procedure. The top image is a microtubule segment, and below is its power spectrum. Figure 2c is the Radon transform of fig. 2b. Each horizontal line in the transform corresponds to the projection along one orientation. Only in the direction perpendicular to the microtubule axis, marked by the arrow in fig. 2c, the projection has a maximum at the central position. A simple peak search along the central column gives the in-plane rotation angle. Peaks also arise from the higher order layer lines and are used for magnification scaling. If these peaks are not clear enough or are more than a preset limit from the expected positions, the segment is rejected. Figure 2d shows the microtubule segment in the proper orientation. Translational alignment of the segments from a given micrograph was then done by cross correlation.

If there is no significant variation in the out-of-plane tilt or axial twist of the microtubule within each image, the rotationally and translationally aligned segments can be averaged to produce an image with good signal to noise ratio. One such average of 28 segments from one microtubule, and its Fourier transform, are shown in fig. 2e and f. Many structural details are visible in this picture, and the Fourier transform of the average clearly includes layer lines up to 4th order with isotropic resolution to at least 10 Å.

We combined the averaged and CTF-corrected data from fourteen microtubule images to produce a 3-D map by weighted back projection. Although this map clearly showed more detail than previous reconstructions, the signal at 10 Å was not substantially higher than in the best of the individual images, so it was apparent that the high resolution data was not being coherently averaged. This problem can be understood by noting that, for a structure of this size, misorientation by two degrees will cause phase errors at 10 Å of about 180 degrees. We expect out-of-plane curvature to produce variations in orientation similar to those seen from in-plane curvature, which can be well over two degrees. Variation of the twist along the microtubule could also be of the same order. None of these variations were taken into account in this initial reconstruction, which was clearly a limiting problem.

#### *Reference-based alignment*

In order to identify the precise orientation of each segment, we turned to a multi-reference-based alignment scheme<sup>17</sup>. Given knowledge of the crystallographic structure of the tubulin dimer and a fair idea of how it fits into the microtubule, we had an opportunity to construct a microtubule reference using the atomic model, with the caveat that we had to ensure that this reference would not bias the reconstruction. There were only two free parameters to be determined in constructing the reference, the radius at which the dimer sits and its rotational angle about the protofilament axis. The procedure used for determining these parameters and producing the reference was as follows.

From each of the 14 microtubule images used to compute the first map, we constructed individual 3-D density maps by back projection. Each map was produced by generating 13 copies of the averaged segment image from a given microtubule to represent 13 different views, with axial shifts to account for the rise after each 13-fold rotational operation. The averaged images of each microtubule had very good contrast, and could be roughly centered by visual inspection. This centering was refined manually after examining the resultant 3-D map (if the image is not exactly centered on the axis, the reconstruction will have high density in the middle where it should be featureless). This method is objective, as the maps were not affected in any way by reference models. The correct protofilament radius was obtained by visually comparing each map with models that were calculated by placing the crystal structure at different radii. The average radius to the dimer center of mass in these 14 reconstructions was 112 Å, in close agreement with the radius of 113 Å obtained from x-ray scattering profiles of the Taxol stabilized microtubules<sup>18</sup>.

In order to determine the protofilament rotational angle, a series of reference models was constructed using the average radius with the crystal structure placed at different angles. The cross-correlation was computed between projections of each of these models and the 14 averages of the microtubule images. The correlation function showed a clear peak at an angle close to that determined in the original docking (fig. 3)<sup>11</sup>. We used the mode that gave the best correlation to generate a set of reference images for the multi-reference alignment.



The reference images were calculated by projecting the model. Projections were taken at one degree intervals covering a range of axial rotational angles of  $1/13$  of a full rotation ( $\sim 28$  degrees) and out-of-plane tilt angles from  $-10$  to  $+10$  degrees, also in one degree steps. At this stage, each individual segment was averaged and reduced to the length of just two monomers. A linear shift of one monomer was applied 13 times, superimposing each of the resultant images to average each segment, and then the center was cut out, making subsequent computational steps faster. Translational parameters and Eulerian angles were obtained for each of the segments from the maximum correlation with the reference projection set.

One objective criterion that can be used to validate the alignment procedure is that both the rotational and tilt angles should change slowly and continuously along the microtubule axis. We set a limit of 3 degrees for the difference in orientation between adjacent segments and excluded those segments whose alignment was not consistent with their neighbors. This procedure resulted in rejection of about 300 of the initial 1500 segments.

### *The microtubule Map at 8 Å resolution*

Data from 89 microtubule images, comprising 1200 segments and about 200,000 monomers, were combined to produce the final map. The map calculation was performed in two steps which avoided the need to generate the 13 equivalent views for each segment. First, back projection was used to reconstruct a map with information from only one asymmetric unit. This map was then symmetrized according to the 13-fold helical operation that places one monomer  $40.6/13$  Å along the axis from the previous one with a rotation of  $4 \times 360/13$  degrees around the axis. Iterative refinement is a standard part of single particle work, but two more cycles of correlation with new reference projections from the previous cycle maps did not result in significant change or improvement. The failure of the map to improve with this type of refinement is understandable as we started out with a very good microtubule model based on the crystal structure.

In order to determine an appropriate curve for scaling the Fourier transform of the reconstruction to compensate for the normal resolution-dependent falloff in amplitudes, we

compared the Fourier transforms of several sections and projections of the map and the reference built from the crystal structure of tubulin. The results are shown in fig. 4. The solid curve is the ratio of amplitudes from projections of the map and model. Ratios of x- and z- sections gave essentially identical curves. The dotted curve is the reciprocal of a 10-point running average of the projection ratio (solid) curve and was used to scale the microtubule map, with a low pass filter that effectively removed frequencies above  $\sim 7$  Å. Over the resolution range from about 40 to 8 Å, the falloff can be approximated by a function of the form  $\exp(-B/d^2)$ , with  $B=75$  Å<sup>2</sup>. The low values of the ratio below 40 Å result from the lack of phase contrast at low spatial frequencies, and the plateau beyond about 8 Å may reflect the noise level in the images.

As a test of the correspondence between our reconstruction and the reference model, we again calculated correlations between the map and various models built with different protofilament rotational angles. The results, shown in fig. 3, demonstrate that the rotation used in the model indeed gives the best fit to the result. To see that the choice of the model did not bias the reconstruction toward that model, a new model with protofilaments rotated 90 degrees was used as the reference in computing a new reconstruction. The resulting map was virtually the same as with the correct model, except for somewhat higher noise level.

Figure 5 shows a contour plot from one section of the final microtubule map. This representation gives a sense of the signal-to-noise ratio as well as the wealth of structural details in the map. Sections through adjacent molecules around the microtubule wall represent views of sections spaced 9.4 Å apart in the axial direction. Alpha helices that run perpendicular to the section are particularly well resolved. Positions of some of the helices in the tubulin structure are marked.

Figure 6 show surface rendered views of the map. Figure 6a is an overall view in which a number of well defined, tubular densities can be seen. This level of detail allows docking of the atomic structure of the protein with a very high degree of precision in the position. Figures 6b and c are views of one dimer in which a ribbon diagram of the crystal structure has been docked, seen from the inside and outside of the microtubule, respectively. Most of the prominent features of the map correspond to helices of the structure, as marked. Except for helix

H6 and the loop that connects it to H7, all of the ribbon diagram fits well within density at the isosurface level used in this figure.

To quantify the accuracy of this docking, the cross correlation between the map and a model density computed from the crystal structure was calculated as the model was moved around within the map, as described earlier<sup>11</sup>. As shown in fig. 3, the rotational angle is well defined to about  $\pm 2$  degrees, while in x, y and z the position is accurate to about 1 Å (data not shown).

The Fourier shell correlation (FSC) and differential phase residual (DPC) are commonly used as measures of resolution in single particle reconstructions by electron microscopy<sup>17,19</sup>. We have calculated these measures of similarity between the experimental density map and the reference model derived from the crystal structure, as shown in fig. 7. The dashed curve indicates the statistically expected error level in the FSC, calculated at 10.8 sigma, which corresponds to the usual 3 sigma curve when the 13-fold symmetry is taken into account. The FSC drops to 0.5 at 9 Å, and crosses the 3 sigma curve at 7 Å, giving two similar values for the resolution according to two criteria in common usage. Also the DPR is below 90 degrees out to about 8 Å. We note that these may be overly conservative measures of resolution, since, as discussed below, we find evidence that the tubulin structure is not precisely the same in the microtubule and crystal.

## Discussion

### *Single particle approach to microtubule structure*

The application of single particle methods to microtubules has allowed averaging of a sufficient number of images to produce a density map, at this resolution of about 8 Å, within which we can identify much of tubulin's secondary structure. Working at a resolution less than about 7 Å allows us to ignore the differences between alpha and beta monomers. Even with some anticipated differences between the crystal and microtubule structures, we can use a reference

for particle alignment that is constructed from the atomic structure. Since this reference is used for alignment of the image segments but not the protofilaments within the segments, the model produces no noticeable bias towards itself in the reconstruction process. On the other hand, calculating the FSC between the model and reconstruction sets an upper limit for the resolution, since the conformation used in making the model is now seen to be not precisely the conformation in the microtubule.

### *Structure of tubulin in microtubules versus zinc-sheets*

A detailed comparison of the structures of tubulin within the microtubule and within the Zn-sheets used to obtain the atomic model can be obtained by docking the crystal structure of the tubulin dimer within our 8 Å microtubule map. At this resolution, alpha helices are readily visible, making docking highly accurate. Figures 8a and b show areas of well defined density (blue mesh) that enclose alpha helical segments (yellow backbone traces). Figure 8a shows the fit of helices 11 and 12, and fig. 8b shows the fit of helices 3, 4 and 5. These regions provide strong constraints for placement of the atomic model and demonstrate that the conformation of tubulin is overall the same in the Zn-sheets and microtubules.

Figure 8c is a view from the inside of the microtubule including the region of the lateral interface between protofilaments. The M-loop, which was previously identified as a critical element in the interface<sup>11</sup>, corresponds to well defined density in the present microtubule reconstruction. However, there are small but significant differences in this region between microtubules and Zn-sheets. The upper part of the M-loop appears to be shifted downwards in the microtubule structure. Conformational differences in this region are expected and are of particular interest, since the inter-protofilament interactions are different in the sheets and microtubules. The downward shifting of part of this loop would result in the widening of the “holes” in the microtubule wall, of potential relevance for understanding the rapid access of ligands to the luminal surface of the microtubule (see below).

Our microtubule reconstruction shows a clear density in the region that is occupied in the atomic model by Taxol in  $\beta$ -tubulin and the B9-B10 loop in  $\alpha$ -tubulin. The location of Taxol

near the M-loop suggested that its stabilizing effect is likely to involve the inducement or stabilization of an M-loop conformation that favors the inter-protofilament interaction<sup>20,21</sup>. In Zn-sheets, the M-loop interacts across the interface with helices H12 and H5, while in microtubules it interacts with helix H3 and the long, N-terminal H1-S2 loop. Although the elements with which the M-loop interacts are completely different in Zn-sheets and microtubules<sup>22</sup>, Taxol has the same stabilizing effect on both. Thus it is likely that the M loop has been fixed by Taxol in similar, extended conformations in both of these polymers.

In Zn-sheets, the H1-S2 loop is poorly resolved. In the electron crystallographic studies of the sheets this long loop was in direct contact with the carbon support in every second protofilament along the sheet. This may have introduced variable distortions resulting in loss of resolution, although the possibility that the loop was disordered to start with cannot be discarded. In our recent refined structure of tubulin we could trace this loop for  $\beta$ -tubulin, but not for  $\alpha$ -tubulin<sup>22</sup>. In the present microtubule map there is very strong density for this part of the structure, as has been seen in previous, lower resolution reconstructions<sup>4-8</sup>. The strong density in this region is most likely due to the stabilization of the H1-S2 loop through its interaction with the M-loop of the neighboring molecule (notice also that in this case there was no carbon support and that this region is close to the lumen and far from any surface that could produce distortion during specimen preparation).

Our studies identify this N-terminal loop as a principal partner of the M-loop for contacts between protofilaments in the microtubule. Figure 8d is an axial view of the interface between protofilaments. The density corresponding to H3 is farther from the M-loop than in our previous docking, resulting from a rotation of the protofilament by about 5 degrees from the orientation described earlier. This orientation, similar to what has been found in more recent work<sup>8,12</sup>, suggests a more peripheral role for H3 in the formation the lateral interface. Figure 9 shows the interacting surfaces of two crystal structures docked into adjacent protofilaments. They are colored to show charge and hydrophobicity of the side chains at the surface. Although some change in the precise conformation of both the M-loop and the H1-S2 loop are expected in the microtubule, the figure shows that there is a fair degree of complementarity across the interface.

Previously we had attributed much of the inter-protofilament interaction to helix H3. We now find that the N-terminal H1-S2 loop (N-loop) plays a more substantive role, which may help to understand some features of dynamics. While most of the differences among tubulin isotypes are found in the C-terminus, there is a cluster of residues in the N-loop region that vary among beta tubulin isotypes. This cluster is positioned just at the region of the inter-protofilament interaction with the M-loop, as shown in fig. 9, and it is possible that the amino acid differences at this point play a critical role in determining the different dynamic properties of the purified isotypes<sup>23</sup> as well as the different sensitivities to drugs such as Taxol<sup>24</sup>. Relating the isotype sequence differences to the different responses to Taxol, in particular, supports the hypothesis that a major part of the effect of Taxol lies in stabilizing a conformation of the M-loop that favors the inter-protofilament interaction. The proximity of these isotype-specific residues to the Taxol binding site suggests that it may eventually be possible to develop isotype-specific drugs that would overcome the clinical problem of drug resistance that arises from alterations in tubulin isotype levels during treatment<sup>25</sup>.

Figures 5, 8c and 9 show that the interaction between protofilaments occurs mainly toward the luminal side of the opposing protofilament surfaces. With the changes in angle that accompany increasing the number of protofilaments in a microtubule, the interactions involving helix H3, H10 and other elements at higher radius become more pronounced. While the increasing surface area involved may contribute to enhanced stability of this interaction, the upper limit in protofilament number may be set by the requirement to maintain the angle small enough to avoid stress on the M-loop – H1-S2-loop interaction.

The most prominent structural difference between the conformation of tubulin in our microtubule structure and the crystallographic model appears at the end of the nucleotide binding region, in helix H6 and the H6-H7 loop. The N-terminal end of H6 is directly in contact with the guanine moiety of the nucleotide, and the helix runs away from the nucleotide binding domain and towards the second domain. Thus this helix is part of a peptide segment that has been proposed to act as a hinge allowing the nucleotide binding domain and the intermediate domain

to rotate following GTP hydrolysis<sup>20,26</sup>. In the crystal structure H6 and the loop connecting it to the core, H7 helix form a small module that is mostly separated from the main body of the monomer. In the Zn-sheets this small domain was well resolved<sup>1</sup>, being stabilized by contacts with helix H4 of the adjacent molecule, and, more importantly, with the upper 3 amino acids of the M-loop<sup>22</sup>. In the microtubule there is no interaction of this segment across the protofilament interface. Furthermore, the microtubule structure suggests that the upper part of the M-loop is shifted downwards, away from H6. The loss of density for H6 and the following loop may be a consequence of this apparent lack of stabilizing contact. Thus it seems that this region may be flexible in the microtubule. Alternatively, there may be some displacement that follows nucleotide hydrolysis in  $\beta$ -tubulin, resulting in different positions for this segment in the two monomers. This hypothesis agrees with the notion that this region is a key in larger conformational differences between the GTP- and GDP-bound forms of tubulin, even though it is positioned at the end of the nucleotide away from the phosphates<sup>20</sup>, but is not supported by the crystal structure, in which this region appears well defined and very similar for both GTP-bound  $\alpha$ -tubulin and GDP-bound  $\beta$ -tubulin.

In conclusion, it seems that in Zn-sheets contacts between the M-loop and helix H6 within the same molecule may stabilize both of them. In microtubules, the M-loop conformation is slightly different so that it loses the contact with H6 rendering the helix more mobile. As an alternative, the lack of the contact of H6 with the adjacent protofilament may result in a flexible H6 region that then does not effectively interact with the M-loop, which then moves down in the microtubule structure. In any case, a flexible H6 module would increase the effective size of the holes in the microtubule wall, enhancing the diffusion of small ligands into the microtubule lumen.

It has been a puzzle that, while Taxol binds to the inside of the microtubule, its binding and exchange rates are extremely rapid. Diaz et al<sup>18</sup> initially proposed that Taxol gets into the microtubule through transient openings between protofilaments, but later saw the same binding speed to microtubule that had been crosslinked and were not expected to fluctuate<sup>27</sup>. The apparent mobility of the H6 module in our present microtubule structure has the consequence

that the pore in the wall is large enough, approximately 17 Å across, to allow the passage of molecules of the size of Taxol.

The small shift of the M-loop in microtubules relative to the Zn-sheets reflects some of the polymorphism in tubulin polymers. It has been reported that when the Zn-sheets roll up to form microtubules, at slightly higher pH, there is an axial offset of about 6 Å between protofilaments<sup>28</sup>. Also, a slight shift in the relative positions of the adjacent protofilaments was observed when Taxol was added to preassembled microtubules<sup>29</sup>. These effects could all be attributed to small shifts in the M-loop.

## Conclusion

The structural design of the microtubule is remarkable in terms of its biological functions. The surface displays a surprisingly large number of binding sites, with numerous MAPs binding to the outside surface and a multitude of small ligands binding to the inside<sup>30</sup>. Our present understanding is that normally dynamics are regulated by proteins that interact with the outside surface or the ends of the microtubule, while the natural compounds that can pass through the wall to bind on the inner surface are generally poisons that may be used in chemical defense. Further characterization of microtubule structure and these binding sites should play an important role in enhancing our understanding of cell cycle control.

The success of our approach to microtubule structure shows that tubular structures can in some cases be better treated as strings of single particles than as helices. This method has great potential for other ordered protein assemblies. With the greatly improved resolution of the present map, we have extended our understanding of the interactions that govern microtubule stability and dynamics. In further studies on microtubules, the methodology serves as a basis for studying the interactions with other proteins, especially in cases where both alpha and beta can be decorated. To reach higher resolution, or work with proteins that decorate the dimer, we will need to be able to distinguish between the alpha and beta monomers. The presence of a seam in



the structure will preclude the 13-fold rotational averaging we have done here, but otherwise the same principles apply.

## Acknowledgements

This work has been supported by NIH grants GM40633 (KHD), GM26357 and GM35433 (DJD), a UC Miller Visiting Professorship (DJD), and the Office of Health and Environmental Research, US Department of Energy, under contract DE-AC03-76F00098.

## Materials and Methods

Tubulin was obtained from Cytoskeleton, Inc. (Denver, CO). Microtubules were polymerized with tubulin at 5 mg/ml in G-PME buffer (80 mM PIPES, 1mM EGTA, 1 mM  $\text{MgCl}_2$ , 1 mM GTP, pH 6.8) in the presence of 50  $\mu\text{M}$  Taxol. After incubation for about 30 min at 37 C, samples were applied to glow-discharged holey carbon films and plunge frozen in liquid ethane. Images were recorded at a magnification of 60,000 on Kodak SO-163 film in a JEOL-4000 electron microscope operating at 400 kV. About half of the images were taken with a defocus of 0.8 – 1.2 mm and half with 1.5 – 2.8  $\mu\text{m}$ . Negatives were examined on an optical bench to identify microtubules showing good resolution. The main criterion for selection was the visibility of the layer line at 20 Å. Selected areas enclosing microtubules were digitized on a PDS-1010M densitometer with step size of 10  $\mu\text{m}$ , corresponding to 1.6 Å on the specimen. Scan sizes were 500 by 5000-8000 pixels. All image processing was carried out with the SPIDER package<sup>31</sup>.

Each microtubule was boxed into small segments of 320 x 320 pixels, including a length of 13 monomers. In each segment, there is a total of  $13 \times 13 = 169$  tubulin monomers, with a total molecular mass of 8.5 MDa.

## Figure Legends

1. Part of a typical microtubule image, recorded with a defocus of about 1  $\mu\text{m}$ . Boxes indicate 320x320 pixel segments that have been cut out of the image.
2. Alignment by Radon transform: a: original image segment; b: power spectrum of a; c: Radon transform of power spectrum; d: segment after rotational alignment; e: average of 28 aligned segments from a different micrograph; f: power spectrum of e.
3. Correlations between experimental maps and models constructed from the atomic structure of tubulin. The dotted curve represents the average correlation between the first 14 microtubule images and projections of the initial models which were calculated with different protofilament rotation angles. The dashed curve shows the correlations between projections of the 10-Å resolution model made by combining the 14 images and the same models. The solid curve shows the correlation between the final microtubule map and a 3-D density map calculated from the crystal structure of the dimer, computed as in ref (11) as the model density is rotated about its axis.
4. Scaling of Fourier transform. Solid curve shows the ratio of averaged transform amplitudes from projections of the map to amplitudes from corresponding projections of the reference model that was derived from the tubulin crystal structure. The dotted curve is the reciprocal of a 10-point running averaging of the projection ratio curve and was used to scale the transform of the microtubule map, with a low pass filter that effectively removed frequencies above  $\sim 7$  Å.
5. Contour plot of one section of the microtubule density map. The section cuts through adjacent monomers 9.4 Å apart along the axis and is viewed looking from the plus end toward the minus end. Positions of alpha helices in the crystal structure are marked..
6. Surface views of the map. a: Overall view, with the plus end of the microtubule toward the top. b, c: Views from the inside and outside, respectively, with a ribbon model of the refined

atomic structure<sup>22</sup> (PDB ID 1JFF) embedded. Helix numbers are marked to aid in orientation. Figure prepared with AVS (Advanced Visual Systems, Inc., Waltham, MA)

7. Resolution evaluation. Fourier shell correlation (FSC) and differential phase residual (DPC) are calculated between the resultant map and the model built from the crystal structure. The dashed curve represents the expected value of the FSC in the absence of signal. For random data, the DPR reaches 104 degrees<sup>19</sup>.

8. Detail of fit between tubulin structure and the map. a: region including helices H11 and H12, corresponding to the outside of the microtubule; b: region of helices H3, H4 and H5, also toward the outside surface; c: view from the inside of the microtubule, showing M- and N-terminal loop region

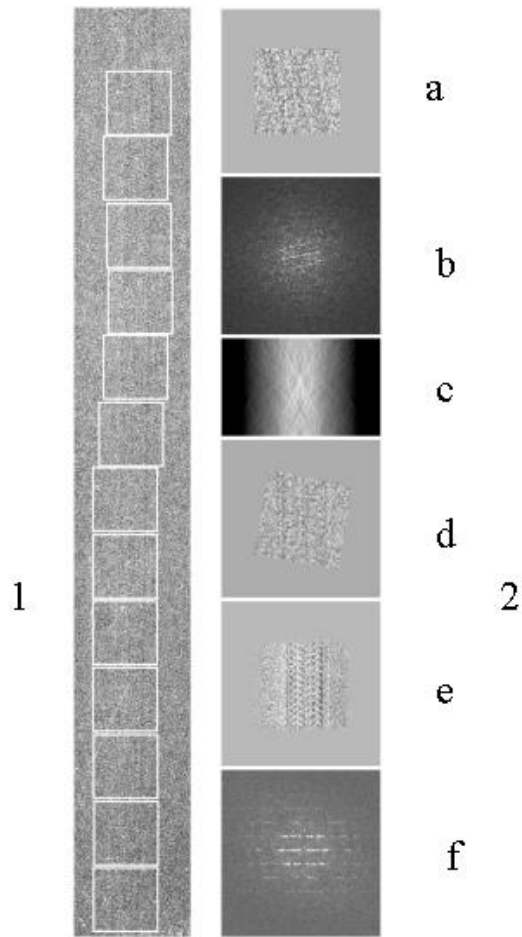
9. Surface of interaction between protofilaments. The protofilaments are rotated 90 degrees apart as indicated to show the M-loop with helices H8, H9 and H10 (right) and N-terminal loop and H3 (left). Regions of each surface of beta tubulin within 5 Å of the opposite surface are colored, red for positively charged side chains, blue for negatively charged, yellow for hydrophobic residues and green for uncharged polar residues. Residues 57-59 are indicated in magenta on the right panel. Figure prepared with Grasp<sup>32</sup>.

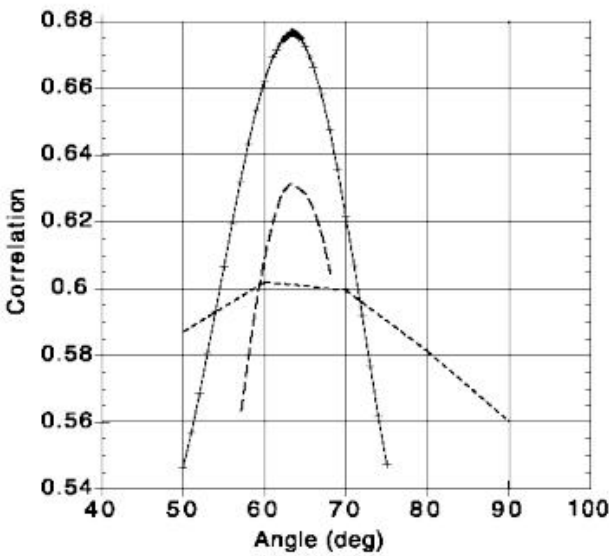
## References

1. Nogales, E., Wolf, S.G. & Downing, K.H. Structure of the  $\alpha\beta$  tubulin dimer by electron crystallography. *Nature* **391**, 199-203 (1998).
2. Nogales, E., Wolf, S.G., Khan, I.A., Ludueña, R.F. & Downing, K.H. Structure of tubulin at 6.5 Å and location of the taxol-binding site. *Nature* **375**, 424-427 (1995).
3. Chrétien, D. & Wade, R. New data on the microtubule surface lattice. *Biol. Cell* **71**, 161-174 (1991).
4. Sosa, H. *et al.* A model for the microtubule-Ncd motor protein complex obtained by cryo-electron microscopy and image analysis. *Cell* **90**, 217-224 (1997).
5. Hoenger, A. *et al.* Image reconstructions of microtubules decorated with monomeric and dimeric kinesins: Comparison with x-ray structure and implications for motility. *J. Cell Biol.* **4**, 419-430 (1998).
6. Arnal, I., Metoz, F., DeBonis, S. & Wade, R.H. Three-dimensional structure of functional motor proteins on microtubules. *Curr. Biol.* **6**, 1265-1270 (1996).
7. Hirose, K., Amos, W.B., Lockhart, A., Cross, R.A. & Amos, L.A. Three-dimensional cryoelectron microscopy of 16-protofilament microtubules: structure, polarity and interaction with motor proteins. *J. Struct. Biol.* **118**, 140-148 (1997).
8. Kikkawa, M., Okada, Y. & Hirokawa, N. 15 Å resolution model of the monomeric kinesin motor, KIF1A. *Cell* **100**, 241-252 (2000).
9. Metoz, F., Arnal, I. & Wade, R. Tomography without tilt: three dimensional imaging of microtubule/motor complexes. *J. Struct. Biol.* **118**, 159- 168 (1997).
10. Sosa, H., Hoenger, A. & Milligan, R.A. Three different approaches for calculating the three dimensional structure of microtubules decorated with kinesin motor proteins. *J. Struct. Biol.* **118**, 149-158 (1997).
11. Nogales, E., Whittaker, M., Milligan, R.A. & Downing, K.H. High resolution model of the microtubule. *Cell* **96**, 79-88 (1999).
12. Meurer-Grob, P., Kasparian, J. & Wade, R.H. Microtubule structure at improved resolution. *Biochemistry* **40**, 8000-8008 (2001).

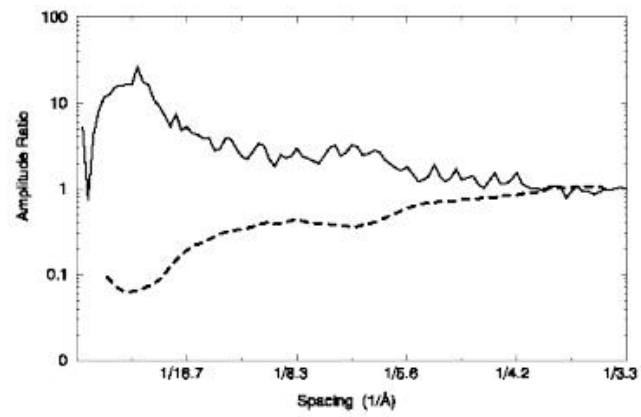
13. Chrétien, D., Metoz, F., Verde, F., Karsenti, E. & Wade, R.H. Lattice defects in microtubules: protofilament numbers vary within individual microtubules. *J. Cell Biol.* **117**, 1031-1040 (1992).
14. Egelman, E.G. An algorithm for straightening images of curved filamentous structures. *Ultramicroscopy* **19**, 367-373 (1986).
15. Radermacher, M. Three-dimensional reconstruction from random projections: orientational alignment via radon transforms. *Ultramicroscopy* **53**, 121-136 (1994).
16. Lanzavecchia, S., Bellon, P.L. & Radermacher, M. Fast and accurate three-dimensional reconstruction from projections with random orientations via radon transforms. *J. Struct. Biol.* **128**, 152-164 (1999).
17. van Heel, M. *et al.* Single-particle electron microscopy: towards atomic resolution. *Quart. Rev. Biophys.* **33**, 307-369 (2000).
18. Diaz, J.F., Valpuesta, J.M., Chacon, P., Diakun, G. & Andreu, J.M. Changes in microtubule protofilament number induced by taxol binding to an easily accessible site - Internal microtubule dynamics. *J. Biol. Chem.* **273**, 33803-33810 (1998).
19. Penczek, P.A., Grassucci, R.A. & Frank, J. The ribosome at improved resolution: new techniques for merging and orientation refinement in 3D cryo-electron microscopy of biological particles. *Ultramicroscopy* **53**, 251-270 (1994).
20. Amos, L. & Löwe, J. How Taxol stabilizes microtubule structure. *Chem. Biol.* **6**, R65-R69 (1999).
21. Snyder, J.P., Nettles, J.H., Cornett, B., Downing, K.H. & Nogales, E. The binding conformation of Taxol in beta-tubulin: A model based on electron crystallographic density. *Proc. Nat. Acad. Sci. USA* **98**, 5312-5316 (2001).
22. Löwe, J., Li, H., Downing, K.H. & Nogales, E. Refined structure of alpha beta-tubulin at 3.5 Å resolution. *J. Mol. Biol.* **313**, 1045-1057 (2001).
23. Ludueña, R.F. The multiple forms of tubulin: different gene products and covalent modifications. *Int. Rev. Cyt.* **178**, 207-275 (1998).
24. Derry, W.B., Wilson, L., Khan, I.A., Ludueña, R.F. & Jordan, M.A. Taxol differentially modulates the dynamics of microtubules assembled from unfractionated and purified  $\beta$ -tubulin isotypes. *Biochemistry* **36**, 3554-3562 (1997).

25. Dumontet, C., Duran, G.E., Steger, K.A., Beketicoreskovic, L. & Sikic, B.I. Resistance mechanisms in human sarcoma mutants derived by single-step exposure to paclitaxel (Taxol). *Cancer Res.* **56**, 1091-1097 (1996).
26. Erickson, H.P. Atomic structures of tubulin and FtsZ. *Trends Cell Biol.* **8**, 133-137 (1998).
27. Diaz, J.F., Strobe, R., Engelborghs, Y., Souto, A.A. & Andreu, J.M. Molecular recognition of Taxol by microtubules - Kinetics and thermodynamics of binding of fluorescent Taxol derivatives to an exposed site. *J. Biol. Chem.* **275**, 26265-26276 (2000).
28. Wolf, S.G., Mosser, G. & Downing, K.H. Tubulin conformation in zinc-induced sheets and microtubules. *J. Struct. Biol.* **111**, 190-199 (1993).
29. Chrétien, D., Flyvbjerg, H. & Fuller, S.F. Limited flexibility of the interprotofilament bonds in microtubules assembled from pure tubulin. *Eur. Biophys. J.* **27**, 490-500 (1998).
30. Downing, K.H. Structural basis for the interaction of tubulin with proteins and drugs that affect microtubule dynamics. *Ann. Rev. Cell Devel. Biol.* **16**, 89-111 (2000).
31. Frank, J. *et al.* Spider and Web - Processing and visualization of images in 3D electron microscopy and related fields. *J. Struct. Biol.* **116**, 190-199 (1996).
32. Nicholls, A., Sharp, K.A. & Honig, B. Protein folding and association - Insights from the interfacial and thermodynamic properties of hydrocarbons. *Proteins-Struct. Funct. Genet.* **11**, 281-296 (1991).

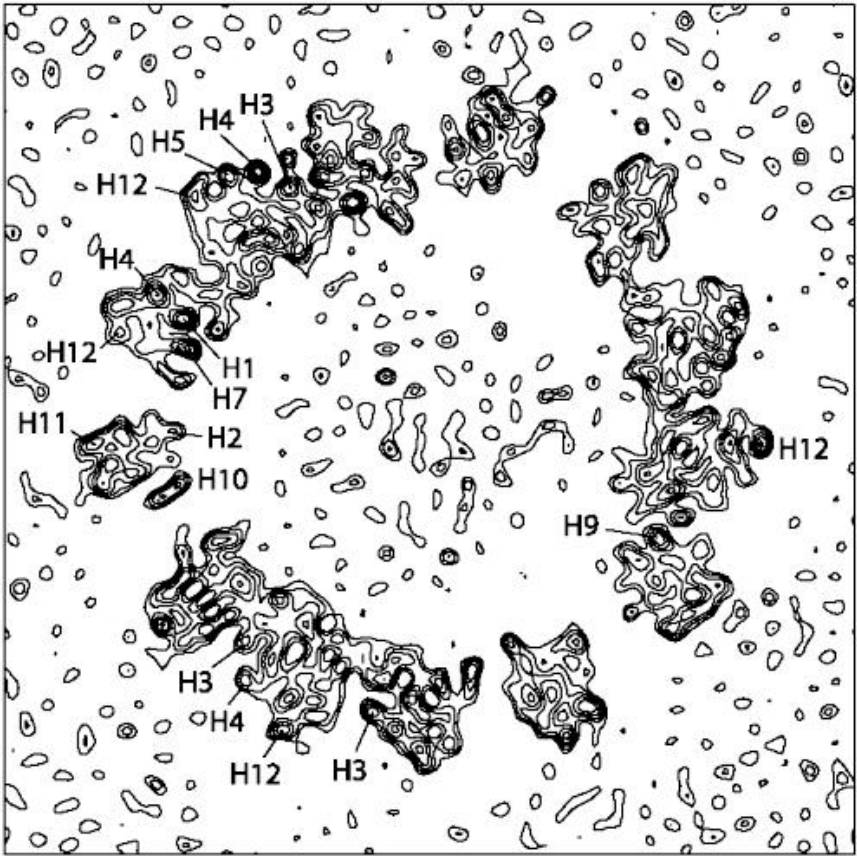


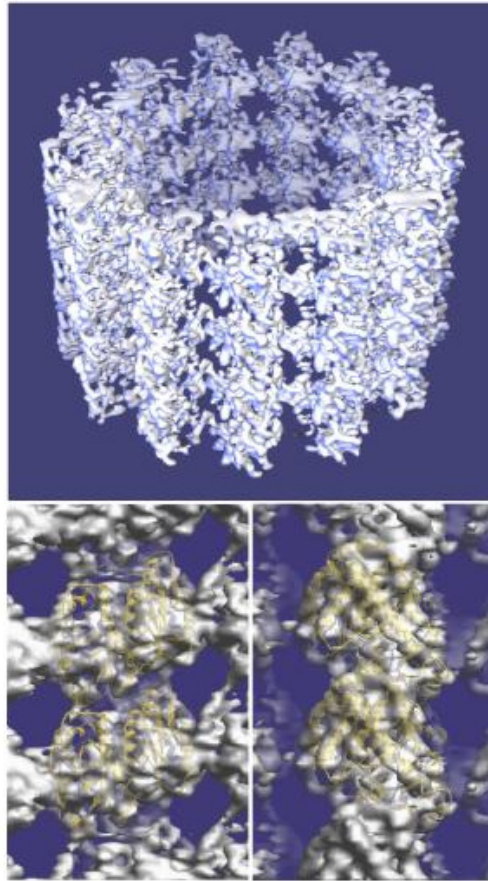




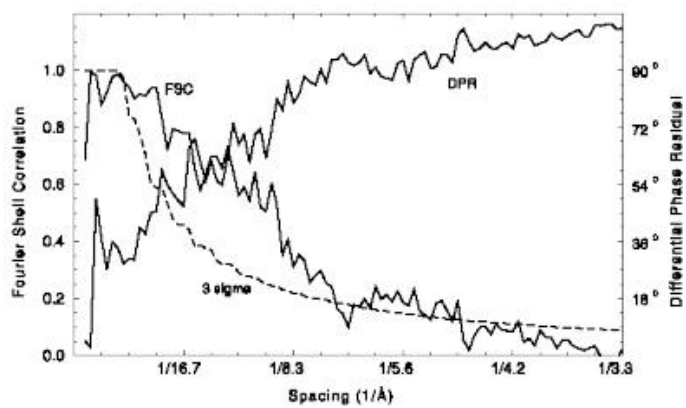


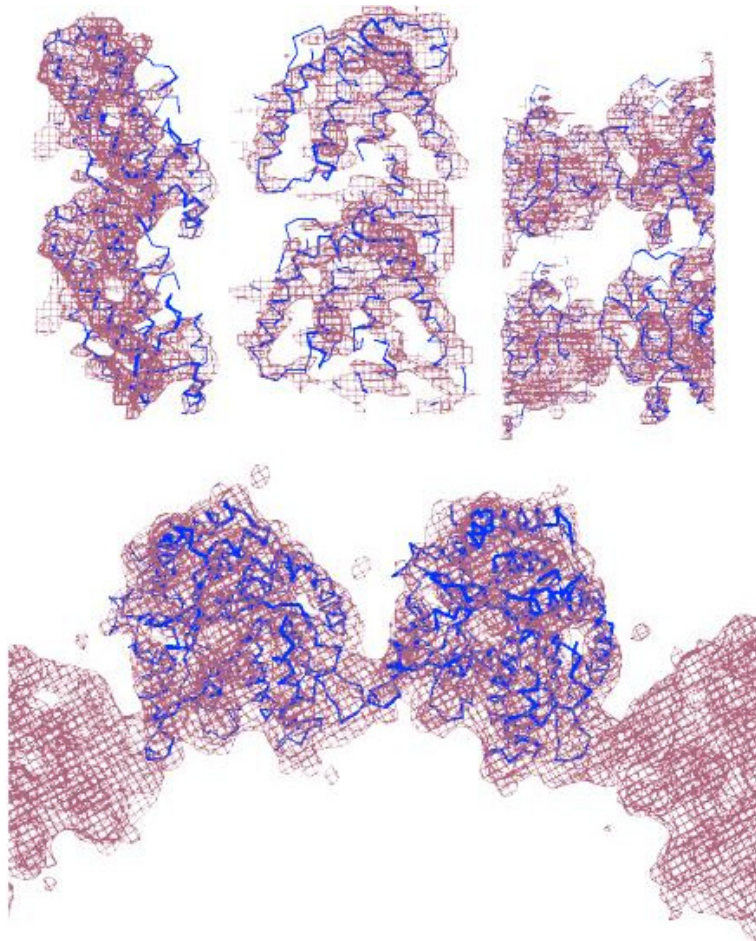
5





6





8

